Capturing the dynamics of Wigner crystals within the phase-field crystal method

Salvador Valtierra Rodriguez,[1] Nan Wang,[2] Nana Ofori-Opoku,[3] Nikolas Provatas,[2] and Kirk H. Bevan[1]
[1]*Division of Materials Engineering, Faculty of Engineering, McGill University, Montreal, QC H3A 0C5, Canada*
[2]*Department of Physics, McGill University, Montreal, QC H3A 2T8, Canada*
[3]*Computational Techniques, Canadian Nuclear Laboratories, Chalk River, ON K0J 1J0, Canada*

(Received 26 November 2018; revised manuscript received 19 November 2019; published 10 December 2019)

An electronic phase-field crystal model is proposed where the thermodynamics of electrons are considered in a free-energy-functional formulation. The free-electron-gas system is considered initially as the noninteracting limit of the model. The excess free-energy contribution to the functional is incorporated by including Coulombic repulsions among electrons and exchange-correlation interactions. The evolution of an electron mean field is considered in the low-temperature limit using diffusive dynamics. Three-dimensional Wigner crystallization can be achieved from the model when the density of the system is lowered sufficiently. Through this approach, we are able to provide insight into topological defect formation and evolution during Wigner crystallization.

DOI: 10.1103/PhysRevB.100.235116

I. INTRODUCTION

The study of Wigner crystals has been of interest to the research community ever since it was first proposed many decades ago [1]. Many analytical and numerical studies have been performed to elucidate the conditions that can stabilize an electron lattice and further our understanding of its properties [2]. Experimentally, the existence of Wigner crystals has been reported in quantum dots, MOSFET devices, dusty plasmas, and even colloids [3–12]. Due to the experimental difficulty associated with generating, controlling, and studying Wigner crystals, a lot of theoretical effort has been dedicated toward understanding their stability and dynamics. Arguably, theoretical Monte Carlo studies have provided the most important insight to date regarding the density range over which Wigner crystals can exist, as well as their dynamic behavior and the existence of other electronic phases [2,13]. Although highly successful, Monte Carlo techniques are computationally limited in the timescales they can analyze. Thus, the study of defect dynamics via Monte Carlo methods is rendered extremely difficult. In this paper, we propose an electronic phase-field crystal (EPFC) formulation for theoretically exploring Wigner crystallization and topological defects across extended timescales.

The analysis of topological defects in these crystals has then been studied through "macroscopic" and "classical" Wigner crystals [11,14,15]. Many of their observations indicate direct similarities with defects observed in crystalline lattices. The first theoretical work on the existence of topological defects in Wigner crystals was developed some decades ago [16]. Electron crystallization has also been explored through density-functional theory (DFT), though primarily from an energetic stability perspective [17]. This approach was preceded by pioneering classical density-functional theory (CDFT) models for studying the solidification of crystals [18]. Eventually, CDFT was combined with ideas from Ginzburg-Landau theories to develop phase-field crystal (PFC) modeling, which we utilize as the basis for modeling electron crystallization in this paper. As a promising mean-field theory, the PFC methodology has been utilized to study phase transitions [19–21]. It has also been successfully used in the past to describe solidification, dislocation and grain-boundary energetics, vapor-liquid phase transitions and certain features of electromigration [20,22,23]. Importantly, the PFC approach allows one to theoretically examine the evolution of topological defects over diffusive timescales.

Herein, we derive a PFC model following the aforementioned electron crystallization DFT approach, where an electron density is employed to construct a free-energy functional and describe the crystallization of an electron fluid [17,18,24]. We view this work as an initial step toward connecting PFC theory with orbital-free density-functional theory (OF-DFT) [25]. For this reason, we focus on developing a 3D electronic structure model. Our development and application of EPFC modeling is detailed in the remainder of this paper. First, we proceed to provide a physical framework for constructing the free energy for a system of electrons (this is provided in Sec. II). From this starting point, a PFC model is then developed in Sec. III. In Sec. IV, the results of topological defect formation and evolution are presented and explained. Next, in Sec. V, we discuss the scope of our approach with respect to OF-DFT and quantum hydrodynamics (QHD). Finally, in Sec. VI, we present our conclusions regarding the EPFC methodology.

II. DENSITY-FUNCTIONAL THEORY APPROACH FOR ELECTRONS

In this paper, we explore a methodology where the free energy (F) of a 3D electron gas may be expressed within the spirit of CDFT as a functional of the electron density (ρ_e). Within CDFT the kinetic-entropic and potential contributions of a system of interacting particles are separated into ideal and excess free-energy terms.

Here, we express the ideal part of the electronic free energy through a Thomas-Fermi kinetic functional that

energetically describes the noninteracting limit in terms of the electron density. Our excess free-energy contribution is described through a Coulombic potential (Hartree term) and an exchange-correlation kernel to account for any other interactions.

This model explores a 3D quantum electron gas system with a positive charge-compensating background jellium where the electron free energy of the system can be well approximated in this manner [26,27]. Through this approach, we define an ideal free energy (F_{id}) associated to a noninteracting system of electrons and an excess free energy (F_{ex}) that deals with the interactions between electrons [28]:

$$F[\rho_e] = F_{\text{id}}[\rho_e] + F_{\text{ex}}[\rho_e]. \tag{1}$$

The energy that describes this system is composed of the kinetic contributions from electrons and the repulsive interaction potential between electrons—while ignoring the energy contribution of the background jellium as a fixed constant and exchange interactions between electrons. A spatially varying formulation of the ideal free energy can be stated as

$$F_{\text{id}}[\rho_e] = \int \left[\frac{3}{5}\alpha\rho_e(\vec{r})^{5/3} - \frac{\pi^2}{4\alpha\beta^2}\rho_e(\vec{r})^{1/3}\right]d\vec{r}, \tag{2}$$

where $\alpha = (3\pi^2)^{2/3}\hbar^2/2m$, $\beta = 1/k_BT$, and $\vec{r}$ is our spatial coordinate; T is the temperature, m is the electron mass, $\hbar$ is Planck's constant, and k_B is Boltzmann's constant. A full discussion regarding the derivation of the entropy term can be found in Refs. [24,26].

Interactions can be captured by introducing an appropriate excess free energy (F_{ex}). It is assumed that direct correlation functions (DCF) can be added to this free energy in the form of an excess free energy to account for the interactions that were ignored earlier in the formulation [17,18,27,29]. These excess free-energy contributions can be obtained in terms of an expansion around some reference state of relevance $\overline{\rho}_e$ [18,30,31]. It is well established that particle interactions can be accounted for by introducing these DCFs [29,30], leading to the following excess free-energy contribution:

$$F_{\text{ex}}[\rho_e] \approx F_{\text{ex}}[\overline{\rho}_e] + \int \left.\frac{\delta F_{\text{ex}}}{\delta\rho_e(\vec{r})}\right|_{\overline{\rho}_e} \delta\rho_e(\vec{r})d\vec{r} + \frac{1}{2}\int d\vec{r}\int \delta\rho_e(\vec{r})\left.\frac{\delta^2 F_{\text{ex}}}{\delta\rho_e(\vec{r})\delta\rho_e(\vec{r}')}\right|_{\overline{\rho}_e} \delta\rho_e(\vec{r}')d\vec{r}'. \tag{3}$$

This formulation for an electron fluid can be understood if the properties of the initial state are known, the Wigner crystal can be described as a highly nonhomogeneous perturbation of the chosen reference state [1,2,17,18,27,32]. Putting together the excess free-energy approximation and the ideal free energy of the electrons yields the Helmholtz free energy of the system. Moreover, the two-point correlation function can be further written in terms of a Coulombic potential and an exchange-correlation kernel $K_{xc}(\vec{r},\vec{r}')$ [17,29,33,34],

$$\frac{\delta^2 F_{\text{ex}}}{\delta\rho_e(\vec{r})\delta\rho_e(\vec{r}')} = -K(\vec{r},\vec{r}') = v(\vec{r},\vec{r}') - K_{\text{xc}}(\vec{r},\vec{r}'), \tag{4}$$

where the exchange-correlation kernel can be evaluated in the jellium limit as a convolution of the Coulombic potential coupling $v(\vec{r},\vec{r}')$ with the exchange-correlation function $g_{\text{xc}}(\vec{r},\vec{r}')$ [28].

III. ELECTRONIC PHASE-FIELD CRYSTAL MODEL FORMULATION

Following the PFC methodology [19–21], let us reformulate our 3D free energy in terms of the rescaled smooth density $n_e(\vec{r}) = [\rho_e(\vec{r}) - \overline{\rho}_e]/\overline{\rho}_e$ and then expand the ideal part of the free energy up to fourth order.

This rescaling (along with another approximation later) is essential given that the original density generates sharp peaks that would require a very fine mesh to simulate. To simplify this task, the ideal free energy will be recast first and the excess free energy later. Considering the electronic ideal free energy, we obtain

$$F_{\text{id}}[n_e] \approx \int\left\{\alpha\overline{\rho}_e^{5/3}\left[\frac{3}{5} + n_e(\vec{r}) + \frac{n_e(\vec{r})^2}{3} - \frac{n_e(\vec{r})^3}{3^3} + \frac{n_e(\vec{r})^4}{3^4}\right]\right\}d\vec{r} - \int\left\{\frac{\pi^2\overline{\rho}_e^{1/3}}{12\alpha\beta^2}\left[3 + n_e(\vec{r}) + \frac{n_e(\vec{r})^2}{3} - \frac{5n_e(\vec{r})^3}{3^3} + \frac{10n_e(\vec{r})^4}{3^4}\right]\right\}d\vec{r}. \tag{5}$$

Here we have expanded the ideal part of the free energy up to fourth order as is typical in the PFC literature [19–21]. For simplicity, let us ignore the temperature-dependent terms in Eq. (5), since the $T = 0$ formulation of the electron gas is generally regarded as reasonably accurate even at room temperature [35]. Higher temperature studies can be found in Refs.[36,37].

Therefore, in this paper, we only endeavor to model Wigner crystal dynamics well below the Fermi temperature. The excess free-energy term $\overline{\mu}_e$ represents the chemical potential of the electron system evaluated at the reference state.

This terms couples linearly to the free energy and given that it is the chemical potential of a homogeneous reference state it can be neglected. One may also identify a couple of terms with the structure of the ideal free energy evaluated at the reference state ($F_{id}[\overline{\rho}_e]$). These terms combined with the excess free energy of the reference state yield the total free energy of the reference state.

We need not in particular specify this free energy and we can merely subtract it from the total free energy, leaving behind a much more compact equation that retains the most essential physics. We then obtain the following total free energy:

$$\mathcal{F}[n_e] = \int\alpha\overline{\rho}_e^{5/3}\left[\frac{n_e(\vec{r})^2}{3} - \frac{n_e(\vec{r})^3}{3^3} + \frac{n_e(\vec{r})^4}{3^4}\right]d\vec{r} + \frac{1}{2}\overline{\rho}_e^2\int d\vec{r}\int\frac{e^2}{4\pi\epsilon_0}\left\{\frac{n_e(\vec{r})n_e(\vec{r}')[1 - g_{xc}(\vec{r},\vec{r}')]}{|\vec{r} - \vec{r}'|}\right\}d\vec{r}', \tag{6}$$

where $\mathcal{F}[n_e] = F[n_e] - F[\overline{\rho}_e]$ is a simplified term for the free energy and e and ϵ_0 are the elementary charge and vacuum permittivity, respectively. This equation highly resembles the one used in DFT, with the central difference arising from the

ideal free-energy term which is a Taylor expansion of the Thomas-Fermi kinetic energy term [24,38].

This expression reflects the linear response of an interacting electron liquid. Linear response functions describe the response of the electronic density due to a perturbation from an external field which can be generalized as the self-consistent response of the electron density to internal fields created by electrons within the same system [33]. Rescaling $\vec{r} = r_s\vec{\tilde{r}}$ and $\vec{r'} = r_s\vec{\tilde{r}'}$ to express the model in dimensionless units,

$$\mathcal{F}[n_e] = \overline{\mu}_F \int \left[\frac{n_e(\vec{\tilde{r}})^2}{3} - \frac{n_e(\vec{\tilde{r}})^3}{3^3} + \frac{n_e(\vec{\tilde{r}})^4}{3^4}\right] d\vec{\tilde{r}} + \left(\frac{e^2}{4\pi\epsilon_0 r_s}\right)\left(\frac{3}{8\pi}\right)\int d\vec{\tilde{r}} \times \int \left\{\frac{n_e(\vec{\tilde{r}})n_e(\vec{\tilde{r}'})[1 - g_{\rm xc}(\vec{\tilde{r}}, \vec{\tilde{r}'})]}{|\vec{\tilde{r}} - \vec{\tilde{r}'}|}\right\} d\vec{\tilde{r}'}, \quad (7)$$

where $\overline{\mu}_F$ is the Fermi energy and r_s is the radius of electron sphere—which is inversely proportional to the density $4\pi r_s^3/3 = 1/\overline{\rho}_e$. From this equation, we can observe a few things. First, the dimensional analysis shows that we have obtained an expression where all the units can be specified through the constant parameters ahead of the integrals.

The scaling of the "density" parameter r_s can also be verified, since $\overline{\mu}_F$ scales as $1/r_s^2$ and the electron interaction terms scale as $1/r_s$, we have obtained the correct scaling reported in literature [24,39]. This is a critical feature, since the crystallization of the Wigner crystal depends on r_s.

To proceed, we must express the Fermi energy in terms of r_s which permits us to directly observe the scalings with respect to r_s and to further simplify the free energy such that

$$\mathcal{F} = \frac{\hbar^2}{2mr_s^2}\left(\frac{9\pi}{4}\right)^{2/3}\int \left[\frac{n_e(\vec{\tilde{r}})^2}{3} - \frac{n_e(\vec{\tilde{r}})^3}{3^3} + \frac{n_e(\vec{\tilde{r}})^4}{3^4}\right] d\vec{\tilde{r}} + \frac{e^2}{4\pi\epsilon_0 r_s}\left(\frac{3}{8\pi}\right)\int d\vec{\tilde{r}}\int \left\{\frac{n_e(\vec{\tilde{r}})n_e(\vec{\tilde{r}'})[1 - g_{xc}(\vec{\tilde{r}}, \vec{\tilde{r}'})]}{|\vec{\tilde{r}} - \vec{\tilde{r}'}|}\right\} d\vec{\tilde{r}'}. \quad (8)$$

If we then multiply both sides of Eq. (8) by $\frac{\hbar^2}{m}(\frac{4\pi\epsilon_0}{e^2})^2$ and keeping in mind the definition of the Bohr radius $a_o = \frac{4\pi\epsilon_0 m}{e^2\hbar^2}$, we obtain

$$\mathcal{F}_o = \frac{a_o^2}{2r_s^2}\left(\frac{9\pi}{4}\right)^{2/3}\int \left[\frac{n_e(\vec{\tilde{r}})^2}{3} - \frac{n_e(\vec{\tilde{r}})^3}{3^3} + \frac{n_e(\vec{\tilde{r}})^4}{3^4}\right] d\vec{\tilde{r}} + \frac{a_o}{r_s}\left(\frac{3}{8\pi}\right)\int d\vec{\tilde{r}}\int \left\{\frac{n_e(\vec{\tilde{r}})n_e(\vec{\tilde{r}'})[1 - g_{xc}(\vec{\tilde{r}}, \vec{\tilde{r}'})]}{|\vec{\tilde{r}} - \vec{\tilde{r}'}|}\right\} d\vec{\tilde{r}'}, \quad (9)$$

where $\mathcal{F}_o$ represents a dimensionless free energy—since our multiplying factor has units of inverse Joules. We can directly observe the correct predicted scaling r_s for both the kinetic and potential of interaction terms [24]. This "new" free energy can be simplified by normalizing by the constant coefficient ahead of the kinetic term and factorizing, thus obtaining

$$\tilde{\mathcal{F}}_o = \int \left[\frac{n_e(\vec{\tilde{r}})^2}{3} - \frac{n_e(\vec{\tilde{r}})^3}{3^3} + \frac{n_e(\vec{\tilde{r}})^4}{3^4}\right] d\vec{\tilde{r}} + \frac{\chi}{2}\int d\vec{\tilde{r}}\int \left\{\frac{n_e(\vec{\tilde{r}})n_e(\vec{\tilde{r}'})[1 - g_{xc}(\vec{\tilde{r}}, \vec{\tilde{r}'})]}{|\vec{\tilde{r}} - \vec{\tilde{r}'}|}\right\} d\vec{\tilde{r}'}, \quad (10)$$

where the dimensionless parameter χ is written as

$$\chi = 2\left(\frac{3}{8\pi}\right)\left[\frac{1}{2}\left(\frac{9\pi}{4}\right)^{2/3}\right]^{-1}\frac{r_s}{a_o}. \quad (11)$$

This final rescaling illustrates the fact that χ is an effective interaction parameter displaying the impact of the density on the system.

In our paper, we utilized the EPFC form provided in Eq. (10) to evolve the electron density and explore Wigner crystallization where an electron fluid solidifies due to a decrease in density that lowers the kinetic energetic contribution of the electrons, which leads to electron-electron interactions being more energetically relevant. We can observe that χ scales linearly with the "density" parameter r_s; this means that as the density is dropped (r_s increases), the electron-electron interactions become stronger compared to the kinetic energy term. We can then rewrite the effective interaction parameter as $\chi \approx 0.12963426(r_s/a_o)$. In literature, the dimensionless "density" parameter (also known as the Brueckner parameter) is used more frequently instead, $r_d = r_s/a_o$. Thus, the final definition of the effective interaction parameter would be $\chi = 0.12963r_d$.

IV. RESULTS

A. 3D local field factor approximation

Simulation of 3D Wigner crystallization was performed to test the model. This required the development of an approximate 3D structure factor, for which the full range of the Brueckner parameter is not available in the literature (to our knowledge). The available data that exists provides the 3D pair distribution function and to some extent, the structure factor for low values of r_d [40,41]. To this end, we proceeded to utilize the results provided in Ref. [42]. For this, we employ the Fourier transform of the 3D pair distribution function and obtain the 3D structure factor for an isotropic, homogeneous system,

$$S(k) = 1 + 4\pi\overline{\rho}_e\int_0^\infty dr\ r^2\frac{\sin(kr)}{kr}h(r), \quad (12)$$

which yields the interacting limit of the structure factor for $r_d = 100$. In this equation, r and k are the radius and wave number, respectively. To obtain the structure factor, further data had to be added to the pair correlation. To accomplish this, a mathematical fitting for the long-range behavior of $g(r)$ was carried out using Eq. (25) in Ref. [2], which allowed us to obtain enough data to compute $S(k)$. Both the data and the model developed so far employ the rescaling $\vec{\tilde{r}} = \vec{r}/r_s$ and $\tilde{k} = kr_s$ thus, Eq. (12) is also rescaled. For the noninteracting limit, we employed the data derived by Ref. [43]. With these two known limits, we generated an approximate local field factor (LFF) such that the essential features of the 3D

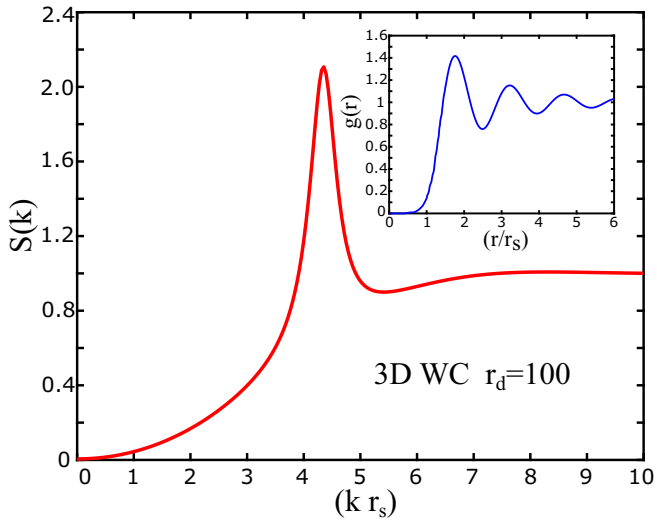

FIG. 1. 3D Structure factor plotted for $r_d = 100$. Inset shows the pair correlation function in Ref. [42].

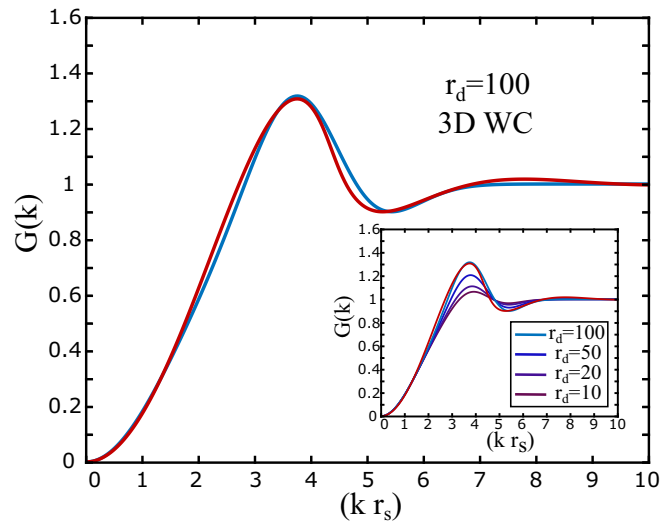

FIG. 2. 3D local field factor (LFF) plotted for $r_d = 100$. The red curve represents the LFF obtained from the data in Ref. [42] while the blue curve is the fitting according to Eq. (14). Inset refers to the LFF for several values of r_d.

structure factor are reproduced (shown in Fig. 1). This was computed from the 3D pair distribution function and the data provided in Ref. [43] for the noninteracting limit. From the literature, it is known that the LFF $G(k)$ provides information on the exchange-correlation energy functional $E_{\rm xc}[n_e]$ and is a convenient measure of exchange-correlation effects [44,45]. We make use of the Singwi, Tosi, Land and Sjolander (STLS) equation to compute our LFF and approximately reproduce the interacting limit [29,46]. In this paper, we limit the scope to the range of densities near the phase transition only [29]:

$$G(k) = -\frac{1}{\overline{\rho}_e}\left(\frac{1}{2\pi}\right)^3 \int d\vec{q}\ \frac{\vec{k}\cdot\vec{q}}{q^2}[S(|\vec{k}-\vec{q}|)-1]. \qquad (13)$$

The employed version of the former equation was also rescaled in the same manner as the structure factor. The 3D LFF is then plotted as shown in Fig. 2. The red line in both plots is the LFF obtained from the data shown in Fig. 1 while the blue line shows the approximation used in this model which will be discussed next. This approach relies heavily on the use of the structure factor of the interacting electron fluid to obtain a fit for the second-order derivative of the excess free energy, something that is also done in PFC, where the first peak of the structure factor showing ordering is located at the first reciprocal lattice vector [20,21]. We can approximate the LFF using a structural PFC (XPFC) approach for fitting the peaks with Gaussian functions [47]. This LFF treatment has also been employed in quantum hydrodynamics [48]. This involved approximating the LFF through a summation of Gaussian functions as shown in Fig. 2. We focus primarily on fitting the data of the first peak. It should be straightforward to note that a sum of Gaussians can yield a fair approximation to the first peaks observed. The use of Gaussians also grants more freedom in the choosing of the position and width of the peaks. The use of Gaussian functions is also a versatile method when dealing with Fourier transforms and convolutions. A single correlation function was employed that depended on the density to approximately fit the LFF, which is explained in more detail in Ref. [29].

An inverse Gaussian is used as reference point to denote the noninteracting limit

$$G(k) = 1 - e^{\frac{-\tilde{k}^2}{w_0^2}} + 0.75Ae^{\frac{-(\tilde{k}-k_1)^2}{w_1^2}} - 0.4Ae^{\frac{-(\tilde{k}-k_2)^2}{w_2^2}}, \qquad (14)$$

where $A = (r_d/r_d^{\max})^{1/2}$ is the amplitude of the Gaussians as a function of r_d and k_i represents the center position of the Gaussians of which k_1 represents the wave number associated to a given reciprocal lattice point. The value $r_d^{\max}$ denotes the relevant range limit in the Brueckner parameter. The constants in the equation are fitted numbers to reproduce the LFF. A similar Gaussian scheme can be found in Ref. [49].

The degree of accuracy of the model can thus be evaluated partly from the essential features of the structure factor that have an impact on crystallization. This approximation is used in conjunction with the Fourier transform of the Coulombic potential to obtain the so-called quantum DCF [2,27,29,50]. This can be observed in the Supplemental Material [51].

These approximations are necessary because adding higher k-modes to the direct correlation function requires a finer mesh which would severely limit the length and timescales that can be explored by the PFC [52]. Further fitting at higher wave numbers in the LFF (and in consequence in the DCF as well) severely impacts the model efficiency, which poses a computational limitation on the system sizes and timescales explored as discussed in Ref. [52]. This is shown in the Supplemental Material, where we have improved this STLS scheme by including a quadratic term that controls the long wave-number behavior [51]. Crystallization is observed as well, albeit at the cost of reducing the volume explored by almost two orders of magnitude and the time spacing by almost an order of magnitude. The DCF of our quadratic fit is also provided in the Supplemental Material to allow further comparison with respect to the literature [51,53]. Although these approximations in the main model do not rigorously reproduce a quadratic behavior in the low wave-

number regime, a Taylor expansion of the noninteracting term does demonstrate a leading quadratic term. Nevertheless, we have found that the STLS scheme LFF given in Fig. 2 can capture the essential physics of Wigner crystallization as will be discussed shortly.

Once the LFF has been approximated, we can simulate the final free energy we obtained using the semi-implicit scheme normally employed in PFC models for the dynamics. To avoid the divergence from the long-range Coulomb interaction, a screened Coulomb potential is employed where the value of the screening wave number is large enough to avoid the divergence but small enough to leave the structure factor largely unaffected. This last consideration is adopted for purely numerical purposes and does not impact the central physics. We employed the diffusive dynamics given by Eq. (15), as well as the subsequent semi-implicit scheme to overcome the time-spacing restriction from finite differences.

B. 3D dynamics and simulations

To simulate topological defect formation and evolution in Wigner crystals, dissipative PFC dynamics are employed [20,21],

$$\frac{\partial n_e}{\partial t} = \nabla^2\left(\frac{\delta \tilde{\mathcal{F}}_o}{\delta n_e}\right) + \eta, \tag{15}$$

where η represents conserved "noise" in the density field. In all our simulations, we utilize the form of the free energy provided in Eq. (10). This equation for the dynamics is solved in Fourier space using a semi-implicit scheme, leading to the following equation [21,29]:

$$\frac{\partial \hat{n}_e}{\partial t} = -|\vec{k}|^2\{\mathrm{FT}[f(n_e)] + \chi v(|\vec{k}|)[1 - G(|\vec{k}|)]\hat{n}_e\} + \hat{\eta}, \tag{16}$$

where $\mathrm{FT}[f(n_e)]$ and $\hat{n}_e$ represent the Fourier transform of the ideal free energy and the density field, respectively. White noise was added to the initial density field to trigger nucleation events as observed in Fig. 3(a). Fluctuations were kept throughout the rest of the simulation via the phenomenological parameter η. The amplitude of the "white" noise employed was 0.012 and was calculated at every grid point of the system. These fluctuations were treated in the same fashion as in standard PFCs [20,21]. This was done with the sole purpose of allowing the system to evolve more rapidly from metastable states [54,55]. A more rigorous approach was not undertaken in the fundamental derivation of these fluctuations, due to the complexity that accompanies the treatment of fluctuations in an electron density field [33]—the reason being that one would need to consider phenomena such as zero-point energy vacuum fluctuations, the wave-function nature of electrons and a more rigorous approach to electron energetics—further information can be found in Ref. [13].

As displayed in Figs. 3(a) and 3(b), the initial state is dominated by random noise perturbations from the reference liquid state with an average of $n_o = 0$. A smaller grid-spacing is employed to simulate the system to better observe the microstructural changes as observed in Fig. 3(a) through 3(h).

The subfigures on the left of Fig. 3 are plotted employing isosurfaces, while those on the right are plotted using slices of the density field (illustrating a 2D representation of the field in any given direction). In Figs. 3(a) and 3(b), these fluctuations generate nucleation events that originate crystal seeds that eventually grow and consume the liquid. In Figs. 3(c) and 3(d), these small seeds collide with each other in a disordered fashion which leads to widespread disorder across the crystal, making it difficult to distinguish any kind of lattice.

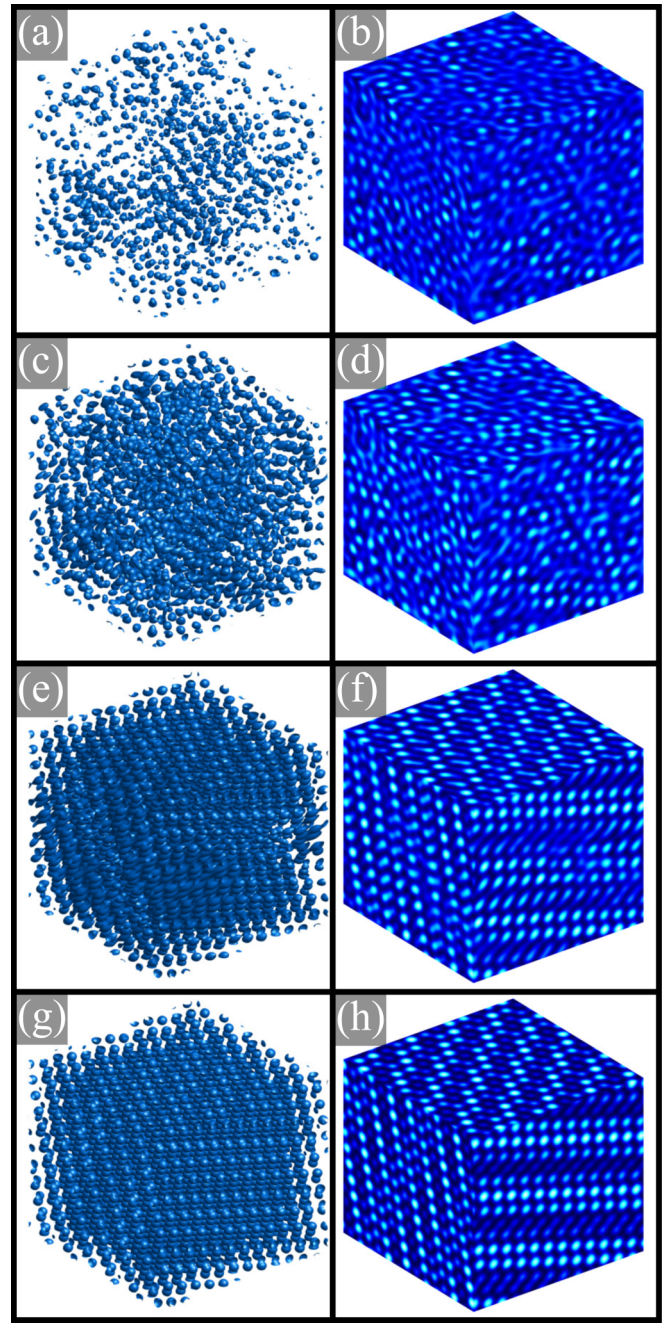

FIG. 3. Solidification of a 3D Wigner crystal in several snapshots: (a), (b) noise is employed as an initial condition; (c), (d) after several seeds nucleate and collide with each other a solid is formed but no distinguishable order can still be observed due to the extensive strain; (e), (f) after some time has elapsed, a fair degree of order can be spotted and the lattice can be observed to be BCC; and (g), (h) once enough time has passed, a considerable amount of strain has been reduced and a highly ordered crystal can be observed.

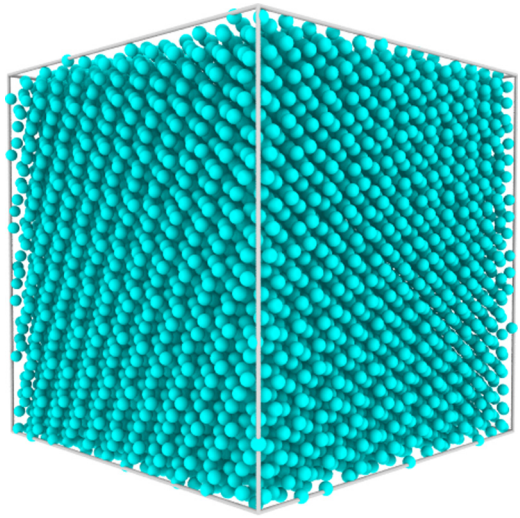

FIG. 4. A common neighbor analysis reveals that the stabilized structure time evolved from a random nucleation process is completely BCC [56,57].

In Figs. 3(e) and 3(f), as the simulation evolves, strain is minimized and a distinguishable lattice starts forming. There are, however, some disorder remnants left which are still being dealt with by the crystal to minimize the strain across the system. In Fig. 3(g), as more time passes, the crystal further relaxes and a very high degree of order can be observed. A very similar situation is found when a stable seed is employed, it starts to grow at the expense of the liquid and covers the whole system in an almost pristine way.

The data visualization and analysis software package OVITO was employed to enable a cleaner display of the structural features of the lattice [56,57]. For visualization purposes, local peaks which represent the most probable particle positions are taken to correspond to particle grid positions. A common neighbor analysis [57] in Fig. 4 shows all the particles and their respective structures in the crystal, demonstrating how the crystal forms a pristine body centered cubic (BCC) configuration (identified only with the blue color, lacking any defects or dislocations).

This same structural analysis approach can be utilized to analyze defect formation and evolution in 3D Wigner crystals as shown in Fig. 5. To more clearly appreciate the evolution of topological defects, crystal seeds were used at the density condition of crystallization. A low-angle grain boundary (LAGB), consisting of an array of edge dislocations, can be generated by setting two seeds right next to each other, slightly rotated in opposite angles as presented in Figs. 5(a) through 5(e). Following our random nucleation study, seed nucleation of the PFC density field is as presented using an isosurface [Figs. 5(a) and 5(c)] and slices of the density field [Figs. 5(b) and 5(d)]. The LAGB is perfectly visualized in both representations by the presence of a Burgers vector and circuit.

It is also possible to structurally discriminate between the ordered (belonging to a BCC lattice) and disordered particles utilizing the common neighbor analysis and the dislocation extraction algorithms [56–58]. Furthermore, we may also

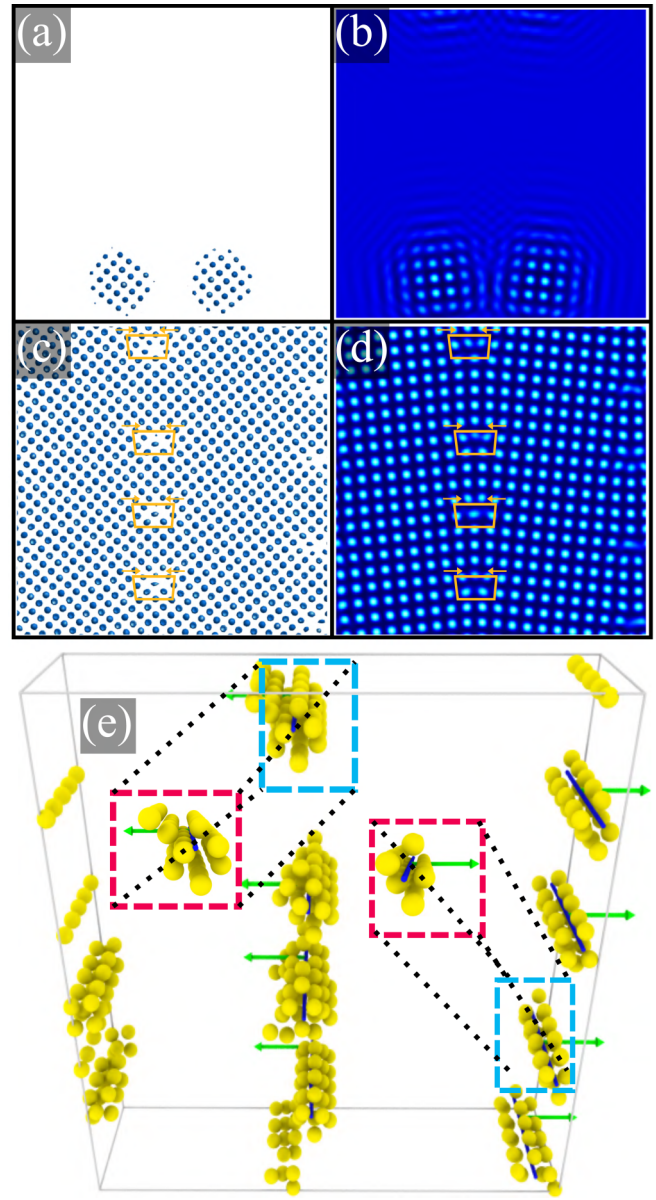

FIG. 5. (a), (b) Two seeds are set in the lower part of a slab system (one of the three dimensions being smaller than the other two, this permits a clearer visualization of defects and the density field). (c), (d) The collision of these two seeds generates a low-angle grain boundary (a linear array of edge dislocations) on both sides (due to the periodicity of the system), however, the ones in the middle being our main focus. (e) Clearer visualization that particularly filters particles with a BCC coordination, leaving only those with irregular coordination (golden color) associated to disorder in the crystal. Also shown are dislocation lines (blue color) which perfectly go through the disordered particles, the Burgers vectors (green color) associated with said dislocations is also displayed.

identify and analyze dislocations in the slab system, ascertain their nature (edge, screw, and/or mixed) and type as illustrated Fig. 5(e). Burgers vectors (green color) and circuits can also be computed for each dislocation and it participating atomic sites (yellow) shown in Fig. 5(e)—yellow atoms participate in a disordered dislocation structure distinct from the perfect BCC phase that would be represented by blue atomic sites as

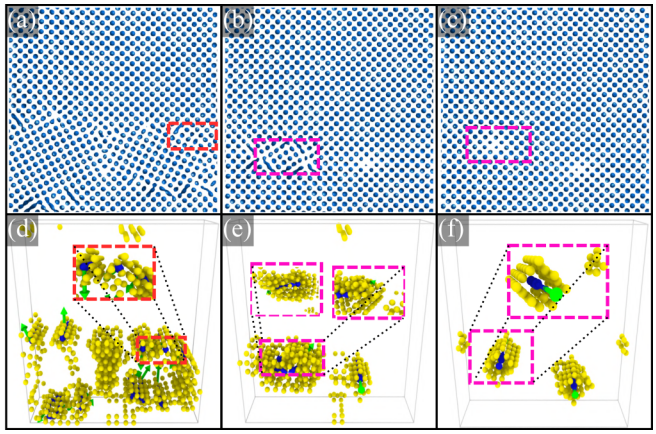

FIG. 6. Upper panels: (a), (d) Several dislocations form from crystal collision. Two neighboring, opposing dislocations (pink box) on the left side of the slab in (b) attract each other and combine into a single dislocation in (c). The Burgers vector (green color) of the new dislocation in (c) is the sum of the vectors of the original dislocations. Lower panels: (d)–(f) are an upper-frontal angle visualization of the dislocations, their direction lines are displayed (blue color), Burgers vectors (green), and their associated, uncoordinated particles (golden particles) as they undergo merging.

in Fig. 4. It is straightforward to observe the Burgers vector is in accordance with the observed array of dislocations from the LAGB density field in Figs. 5(c) and 5(d). The nature of all dislocations is also displayed in the slab system [dark blue atoms in Fig. 5(e)] and identified to be an edge nature. This is in accordance with the type of dislocation that is generated by a LAGB.

Fisher *et al.* first explored the possibility of topological defects in Wigner crystals decades ago [16]. More recent work on mesoscopic and macroscopic "Wigner crystals" has also yielded interesting information about possible defects [11,14,15]. Special attention was given by them as well as more modern research regarding the evolution of grain boundaries and dislocations [14].

Finally, we explore how dislocations can combine within Wigner crystals across extended timescales. For this simulation, a third seed was added to the previous simulation in the center of the slab with the purpose of generating a collision with the other seeds and producing scattered dislocations across the domain. The system is allowed to relax for a certain period of time until a few dislocations remain. This permits a suitable situation for the proper visualization of the dislocation motion and interaction.

In Fig. 6(a), several dislocations are displayed, some of these undergo merging and a simpler configuration of three neighboring dislocations is obtained in Fig. 6(b). Two dislocations [bounded by pink boxes in Fig. 6(e)] attract each other due to their opposing Burgers vectors (any two dislocations will experience an attractive force if their unitary vectors are opposite). Their respective Burgers vector and orientation are also displayed utilizing the approach discussed above [56–58]. The upper and lower subfigures in Fig. 6 present the time-evolved snapshots of the PFC density field and particle structural visualization, respectively. The two relevant dislocations attract each other and leave behind a perfect dislocation after merging as displayed in Figs. 6(c) and 6(f)—whose Burgers vector (green) is the total sum of the Burgers vectors of the initial dislocations. The larger insets in the lower panels represent zoomed versions of the identified dislocations. This demonstrates that dislocation interactions follow conservation of the Burgers vector in Wigner crystals. The vectors identified for the two relevant dislocations are $1/2[\bar{1}\bar{1}\bar{1}]$ and $1/2[\bar{1}11]$ and the resultant observed in the new dislocation is $[\bar{1}00]$. This behavior has been observed for "classical Wigner crystals" in charged particles in colloids experiments [11]. In said experiments, other defects such as grain boundaries were also reported.

V. RELATIONSHIP WITH OTHER METHODS

This model can directly draw analogies to OF-DFT schemes that deal with an approximate kinetic energy functional—avoiding the direct use of wave functions. In OF-DFT, functional approximations are also assumed for the exchange-correlation energy terms [25]. The minimization of an energy functional in OF-DFT, while preserving the number of electrons in a fixed volume, also draws an analogy to our work. Here we also minimize an energy functional while using a Laplacian to run diffusive electron dynamics, as well as preserving the number of electrons and volume. A self-consistent converging OF-DFT algorithm seeking the ground state has an analogous role to the one in our dynamics, in which we can observe the initial (out-of-equilibrium) state trying to reach the equilibrium state. Indeed, we view our work as an initial step toward connecting OF-DFT and PFC methods.

Another comparison to our work can be drawn with QHD. For example, in Ref. [48], a functional of the electron density is also minimized and it is proposed that the effects of exchange and correlation be accounted for by using a LFF [48,59]. The dynamics employed evolve not only the electron density field, but also a velocity field as is typical in hydrodynamic techniques. In terms of energetics, our approach and QHD can be very similar due to the Thomas-Fermi approach QHD can adopt—if one ignores terms coupling the velocity and density fields in QHD. Similarities between QHD and our EPFC model also include the use of Gaussians as well to parametrize and describe the LFF (see Ref. [48]). Thus, from a purely energetics perspective, QHD and the work presented herein are close.

That being said, EPFC dynamics and the results obtained from QHD would still differ. The dynamics employed in QHD, while very similar for the mass conservation equation, can be distinguished by the presence of the coupling to the velocity field. This coupling is difficult to accommodate in the EPFC model, since the dynamics allow the density field to oscillate at the interparticle level while the velocity field normally deals with a smooth field. In addition, density oscillations at the interparticle level would lead to strong gradients that could produce unphysical flows. Meaning, velocity variations at the interparticle level are not a straightforward matter [59]. Thus, PFC dynamics are not identical to quantum hydrodynamics.

VI. CONCLUSIONS AND DISCUSSION

An EPFC formulation for the modeling electron thermodynamics in 3D Wigner crystals was developed starting from a CDFT-type separation of the electron free energy into ideal and excess free-energy functional terms. This CDFT approach to treating the electrons was developed and well explained in the work of Senatore *et al.* and Louis *et al.* who provide an energy functional for the interacting electron system [28,29].

Subsequently, the functional was cast in a PFC-type form and correlations were introduced in an XPFC-like approach. Several approximations were employed in the development of this model, such as the expansion of the kinetic functional (ideal free energy term); the use of rescaled, smooth electron density, and the mean-field treatment of the derivatives of the excess free energy, as well as the Gaussian fit employed to treat the local-field correction factor. Despite these approximations, the model recovers the correct scalings with respect to critical parameters. This includes the dimensionless "density" parameter r_d, which in conjunction with a constant coefficient, becomes the effective interaction parameter χ. The effective interaction parameter compares the strength of the potential energy of interaction to that of the kinetic energy of the electrons.

A value of $r_d = 162$ was found for the 3D simulations within the STLS approximations applied, outside the expected value of 100 ± 20 reported in QMC literature for 3D Wigner crystals. This might be due to the Taylor expansion of the kinetic term, the approximate treatment of the LFF, and/or inherent limitations of the approach we here employ. However, a k^2 asymptotic correction of the LFF yields a significant improvement of this value to $r_d = 140$.

Crucially, the formation of a Wigner crystal in our EPFC model is obtained through the use of a Coulombic potential and XPFC-like phenomenological fit of the exchange-correlation kernel (through the LFF) in Fourier space. This approach permits one to retain the most essential physics of crystallization and defect dynamics, while keeping a connection with quantum-mechanical formulations. We emphasize that these approximations were done to arrive at tractable topological simulations in the time and length scales of interest (nucleation through to full crystallization), resulting in a model that is tractable in terms of computational resources. This was observed as the more accurate k^2 asymptotic correction scheme requires smaller grid and time spacing. An interesting observation is that the features and curvature of the LFF between the first peak and the k^2 asymptotic transition modestly influences the crystallization value. A minor innovation is the inclusion of a negative Gaussian after the first peak in the LFF, something that hadn't been done previously in XPFC schemes. The formation of defects is expected, as it is well known that whenever a free-energy functional is minimized by a periodic structure, this will naturally introduce elasticity to the model, which in turn will permit the existence of defects [19–21].

This behavior has also been reported for macroscopic and classical Wigner crystals, which offer a close comparison to our work regarding the dynamics of observed defects [14,15]. We demonstrate the presence and dynamics of dislocations and grain boundaries whose behavior is consistent with theoretical and/or experimental research. Overall, the results provided by our EPFC model match well with both experimental and theoretical literature. In conclusion, this paper establishes a promising path connecting 3D electron thermodynamics and PFC modeling through Wigner crystallization. We have shown how the latter may be studied, starting from a CDFT-type formalism, separating out ideal and excess free-energy terms, followed by an extension to a mean-field PFC-like approach. Through an XPFC-type correlation approximation, we were able to obtain a computationally tractable model. This model provides a promising tool for studying topological defect formation and evolution in Wigner crystals over diffusive timescales. Future work could focus on more deeply exploring the phase diagram of Wigner crystals, via EPFC-type methods. Spin polarization can also be studied as magnetism has been studied in PFC models as well [60]. More concrete quantum derivations regarding the phenomenological fluctuation terms utilized could also be provided. We further envision the next step in the development of this model would be to establish a direct dynamical connection between OF-DFT and PFC modeling, permitting direct comparison.

ACKNOWLEDGMENTS

We wish to acknowledge financial support that made this research possible from Consejo Nacional de Ciencia y Tecnología (CONACYT), Mexico, Natural Sciences and Engineering Research Council of Canada (NSERC), and the McGill Engineering Doctoral Awards (MEDA) Program. Computational support was provided by Compute Canada and Calculc Quebec, through the Canadian Foundation for Innovation. The authors also wish to acknowledge the valuable discussions with the McGill Physics Computational Materials Science Group. The atomic visualization and analysis packages OVITO, the Common Neighbor Analysis, and the Dislocation Extraction Algorithm (DXA) were used in this work [56–58].

[1] E. Wigner, Phys. Rev. **46**, 1002 (1934).
[2] B. Tanatar and D. M. Ceperley, Phys. Rev. B **39**, 5005 (1989).
[3] S. V. Kravchenko, G. V. Kravchenko, J. E. Furneaux, V. M. Pudalov, and M. D'Iorio, Phys. Rev. B **50**, 8039 (1994).
[4] M. P. Sarachik and S. V. Kravchenko, Proc. Natl. Acad. Sci. U.S.A. **96**, 5900 (1999).
[5] A. Prinz, V. Pudalov, G. Brunthaler, and G. Bauer, Superlattices Microstruct. **27**, 301 (2000).
[6] B. Spivak, Phys. Rev. B **67**, 125205 (2003).
[7] J. H. Chu and L. I. Phys. Rev. Lett. **72**, 4009 (1994).
[8] H. Thomas, G. E. Morfill, V. Demmel, J. Goree, B. Feuerbacher, and D. Möhlmann, Phys. Rev. Lett. **73**, 652 (1994).
[9] H. C. Lee and B. Rosenstein, Phys. Rev. E **55**, 7805 (1997).
[10] M. Bonitz, P. Ludwig, H. Baumgartner, C. Henning, A. Filinov, D. Block, O. Arp, A. Piel, S. Käding, Y. Ivanov, A. Melzer, H. Fehske, and V. Filinov, Phys. Plasmas **15**, 055704 (2008).
[11] W. T. M. Irvine, A. D. Hollingsworth, D. G. Grier, and P. M. Chaikin, Proc. Natl. Acad. Sci. USA **110**, 15544 (2013).

[12] F. Bolton and U. Rössler, Superlattices Microstruct. **13**, 139 (1993).

[13] R. Martin, L. Reining, and D. Ceperley, *Interacting Electrons: Theory and Computational Approaches* (Cambridge University Press, New York, 2016).

[14] A. Radzvilavičius and E. Anisimovas, J. Phys.: Condens. Matter **23**, 385301 (2011).

[15] M. Saint Jean, C. Guthmann, and G. Coupier, Eur. Phys. J. B **39**, 61 (2004).

[16] D. S. Fisher, B. I. Halperin, and R. Morf, Phys. Rev. B **20**, 4692 (1979).

[17] G. Senatore and G. Pastore, Phys. Rev. Lett. **64**, 303 (1990).

[18] T. V. Ramakrishnan and M. Yussouff, Phys. Rev. B **19**, 2775 (1979).

[19] K. R. Elder and M. Grant, Phys. Rev. E **70**, 051605 (2004).

[20] K. R. Elder, N. Provatas, J. Berry, P. Stefanovic, and M. Grant, Phys. Rev. B **75**, 064107 (2007).

[21] N. Provatas and K. Elder, *Phase-Field Methods in Materials Science and Engineering*, 1st ed. (Wiley-VCH, Weinheim, Germany, 2010).

[22] G. Kocher and N. Provatas, Phys. Rev. Lett. **114**, 155501 (2015).

[23] N. Wang, K. H. Bevan, and N. Provatas, Phys. Rev. Lett. **117**, 155901 (2016).

[24] R. Martin, *Electronic Structure: Basic Theory and Practical Methods* (Cambridge University Press, Cambridge, England, 2004).

[25] Y. A. Wang and E. A. Carter, *Theoretical Methods in Condensed Phase Chemistry* (Springer, Dordrecht, Netherlands, 2002), Chap. 5, pp. 117–184.

[26] K. Huang, *Statistical Mechanics* (John Wiley & Sons, Inc., New York, 1987).

[27] M. Rovere, G. Senatore, and M. P. Tosi, Ordering transitions induced by Coulomb interactions, in *Progress in Electron Properties of Solids: Festschrift in Honour of Franco Bassani* (Springer, Dordrecht, Netherlands, 1989), pp. 221–238.

[28] A. Louis, H. Xu, and J. Anta, J. Non-Cryst. Solids **312-314**, 60 (2002).

[29] S. Moroni and G. Senatore, Phys. Rev. B **44**, 9864 (1991).

[30] J. Hansen and I. McDonald, *Theory of Simple Liquids* (Academic Press, London, England, 2013), 4th ed.

[31] C. E. Starrett and D. Saumon, Phys. Rev. E **85**, 026403 (2012).

[32] S. Moroni and G. Senatore, J. Phys.: Condens. Matter **2**, SA139 (1990).

[33] G. Giuliani, G. Vignale, and C. U. Press, *Quantum Theory of the Electron Liquid*, Masters Series in Physics and Astronomy (Cambridge University Press, Cambridge, UK, 2005).

[34] S. Moroni, D. M. Ceperley, and G. Senatore, Phys. Rev. Lett. **75**, 689 (1995).

[35] D. Griffiths, *Introduction to Quantum Mechanics* (Pearson Prentice Hall, Upper Saddle River, NJ, 1995).

[36] S. Groth, T. Dornheim, and J. Vorberger, Phys. Rev. B **99**, 235122 (2019).

[37] T. Dornheim, J. Vorberger, S. Groth, N. Hoffmann, Z. A. Moldabekov, and M. Bonitz, J. Chem. Phys. **151**, 194104 (2019).

[38] S. Datta and C. U. Press, *Quantum Transport: Atom to Transistor* (Cambridge University Press, New York, 2005).

[39] N. Ashcroft and N. Mermin, *Solid State Physics*, HRW international ed. (Holt, Rinehart and Winston, New York, 1976).

[40] T. Dornheim, S. Groth, J. Vorberger, and M. Bonitz, Phys. Rev. E **96**, 023203 (2017).

[41] S. Groth, T. Dornheim, and M. Bonitz, J. Chem. Phys. **147**, 164108 (2017).

[42] L. Cândido, B. Bernu, and D. M. Ceperley, Phys. Rev. B **70**, 094413 (2004).

[43] T. Dornheim, S. Groth, and M. Bonitz, Contrib. Plasma Phys. **57**, 468 (2017).

[44] G. Senatore, S. Moroni, and D. Ceperley, J. Non-Cryst. Solids **205-207**, 851 (1996).

[45] B. Davoudi, M. Polini, G. F. Giuliani, and M. P. Tosi, Phys. Rev. B **64**, 153101 (2001).

[46] K. S. Singwi, M. P. Tosi, R. H. Land, and A. Sjölander, Phys. Rev. **176**, 589 (1968).

[47] M. Greenwood, N. Provatas, and J. Rottler, Phys. Rev. Lett. **105**, 045702 (2010).

[48] Z. A. Moldabekov, M. Bonitz, and T. S. Ramazanov, Phys. Plasmas **25**, 031903 (2018).

[49] M. Corradini, R. Del Sole, G. Onida, and M. Palummo, Phys. Rev. B **57**, 14569 (1998).

[50] S. Tanaka, J. Chem. Phys. **145**, 214104 (2016).

[51] See Supplemental Material at http://link.aps.org/supplemental/10.1103/PhysRevB.100.235116 for a more detailed model derivation, direct correlation functions, and k^2 correction crystallization.

[52] J. Berry, N. Provatas, J. Rottler, and C. W. Sinclair, Phys. Rev. B **86**, 224112 (2012).

[53] C. N. Likos, S. Moroni, and G. Senatore, Phys. Rev. B **55**, 8867 (1997).

[54] C. Maier, T. Brydges, P. Jurcevic, N. Trautmann, C. Hempel, B. P. Lanyon, P. Hauke, R. Blatt, and C. F. Roos, Phys. Rev. Lett. **122**, 050501 (2019).

[55] J. Berry, K. R. Elder, and M. Grant, Phys. Rev. B **77**, 224114 (2008).

[56] A. Stukowski, Modell. Simul. Mater. Sci. Eng. **18**, 015012 (2009).

[57] J. D. Honeycutt and H. C. Andersen, J. Phys. Chem. **91**, 4950 (1987).

[58] A. Stukowski, V. V. Bulatov, and A. Arsenlis, Modell. Simul. Mater. Sci. Eng. **20**, 085007 (2012).

[59] V. Heinonen, C. V. Achim, J. M. Kosterlitz, S.-C. Ying, J. Lowengrub, and T. Ala-Nissila, Phys. Rev. Lett. **116**, 024303 (2016).

[60] M. Seymour, F. Sanches, K. Elder, and N. Provatas, Phys. Rev. B **92**, 184109 (2015).